Available online at www.sciencedirect.com
ScienceDirect
European Journal of Mechanics B/Fluids 27 (2008) 268–289

Variable density and viscosity, miscible displacements in capillary tubes

S.H. Vanaparthy, E. Meiburg *

Department of Mechanical Engineering, University of California, Santa Barbara, CA 93106, USA

Received 20 March 2007; received in revised form 14 June 2007; accepted 14 June 2007

Available online 20 July 2007

Abstract

The displacement of a more viscous fluid by a miscible, less viscous one of lower density in a horizontal capillary tube is studied by means of Stokes flow simulations. Both axisymmetric and three-dimensional simulations are conducted at Péclet numbers up to 10^4, in order to resolve discrepancies between earlier simulations by [C.Y. Chen, E. Meiburg, Miscible displacements in capillary tubes. Part 2. Numerical simulations, J. Fluid Mech. 326 (1996) 57] and corresponding experiments of [P. Petitjeans, T. Maxworthy, Miscible displacements in capillary tubes. Part 1. Experiments, J. Fluid Mech. 326 (1996) 37] and [J. Kuang, T. Maxworthy, P. Petitjeans, Miscible displacements between silicone oils in capillary tubes, Eur. J. Mech. B Fluids 22 (2003) 271–277]. An initial set of simulations addresses the influence of different viscosity–concentration relations on the quasisteady finger tip velocity. The results indicate that steeper relations generally result in a higher tip velocity. However, the effect is too small to explain the above discrepancies. Further simulations show that a concentration-dependent diffusion coefficient results in a slight reduction of the tip velocity at moderate *Pe*, but again the effect is too small to fully account for the observed differences.

Three-dimensional simulations that include gravitational forces yield a much more significant effect. Consistent with the experiments of [P. Petitjeans, T. Maxworthy, Miscible displacements in capillary tubes. Part 1. Experiments, J. Fluid Mech. 326 (1996) 37], at moderate *Pe* the tip slows down as the gravity parameter increases, an effect that becomes more pronounced as *Pe* decreases. However, the three-dimensional simulations do not produce the longitudinal splitting phenomenon observed by [P. Petitjeans, T. Maxworthy, Miscible displacements in capillary tubes. Part 1. Experiments, J. Fluid Mech. 326 (1996) 37]. In order to check for the existence of gravitational instabilities that might cause such a splitting, additional two-dimensional simulations are conducted in cross-sections of the tube. A comparison of these two-dimensional results with corresponding three-dimensional simulations demonstrates that for a wide range of parameters the evolution of the trailing finger sections is governed by a two-dimensional balance between gravitational and viscous forces. However, a gravitational instability along the lines suggested by [P. Petitjeans, T. Maxworthy, Miscible displacements in capillary tubes. Part 1. Experiments, J. Fluid Mech. 326 (1996) 37] was not observed. On the other hand, for some parameter combinations the evolution of a 'dimple' is observed on the lower side of the finger, and close to its tip. This dimple may signal the evolution of a splitting phenomenon after long times, which are beyond the reach of the current simulations. Taken together, the two- and three-dimensional simulations suggest that the splitting phenomenon observed by [P. Petitjeans, T. Maxworthy, Miscible displacements in capillary tubes. Part 1. Experiments, J. Fluid Mech. 326 (1996) 37] likely is caused by the gravity-induced modification of the flow around the tip of the finger, rather than by a gravitational instability per se.

* Corresponding author.
E-mail address: meiburg@engineering.ucsb.edu (E. Meiburg).

0997-7546/$ – see front matter
doi:10.1016/j.euromechflu.2007.06.003

Keywords: Miscible displacement; Variable viscosity and density; 3D simulations

1. Introduction

The displacement of a viscous fluid by another one of different viscosity and density represents a problem of fundamental interest. It finds applications in situations ranging from enhanced oil recovery and the spreading of pollutants in groundwater reservoirs, to pipeline lubrication and processes in the chemical industry. Simple geometries such as Hele–Shaw cells or capillary tubes have frequently been employed to gain an understanding of the mechanisms governing these flows. Instabilities can give rise to complex dynamics of such displacements, for example in core-annular capillary tube flows [1–3], or when a less viscous fluid displaces a more viscous one in a porous medium [4,5].

The classical investigations by [6] and [7] consider the situation in which a viscous fluid is expelled from a capillary tube by a second, inviscid fluid with which it is immiscible. A quasisteady finger of the inviscid fluid forms and propagates along the center of the tube. Its tip velocity is directly related to the fraction of the viscous fluid left behind on the tube wall, which the authors determine as a function of a suitably defined capillary number. Subsequent numerical calculations by [8] show good agreement with the experimental observations. More recently, this work was extended to finite viscosity ratios by [9], and to non-Newtonian fluids by [10].

The miscible variant of this problem was first addressed in the companion papers by [1], who conducted experiments for water/glycerin mixtures, and [11], who performed corresponding axisymmetric simulations. [12] and [13] extend the findings of [1] to mixtures of silicone oils, cf. also the related work of [14]. At high Péclet numbers Pe, and for all viscosity ratios, the axisymmetric simulations of [11] were seen to be in good agreement with the corresponding experiments regarding the fraction of the more viscous fluid left behind on the walls. For moderate values $Pe < \mathrm{O}(10^4)$, on the other hand, significant differences surfaced. Specifically, the experiments, which were conducted in horizontal capillary tubes of different diameters, showed a substantial reduction in the quasisteady finger tip velocity for decreasing Péclet numbers, while the simulations did not observe such a significant influence of Pe. The goal of the present investigation is to resolve these discrepancies between the experiments and the axisymmetric simulations. Towards this end, we will explore several potential reasons. A first point to be mentioned in this context is that the simulations of [11] were limited to fluid combinations characterized by an exponential relation between viscosity and concentration. In contrast, [1] found that for the water and glycerin mixtures employed in their experiments, this relation is better described by a double exponential function. In order to explore the importance of the viscosity–concentration relation on the tip velocity in a more general fashion, we will investigate several different families of viscosity–concentration relations.

A second point concerns the assumption of a constant diffusion coefficient in the simulations of [11]. The experimental measurements by [1] demonstrate that for water and glycerin the diffusion coefficient varies strongly with the concentration, which was confirmed in the recent work of [15]. [11] briefly consider this issue by assuming a linear variation of the diffusion coefficient with concentration in their simulations. However, this implementation failed to yield a quasisteady tip velocity when the same dimensionless parameter values were employed as in the experiments. Hence, we will conduct an analysis of the influence of a concentration-dependent diffusion coefficient, based on the more realistic Stokes–Einstein relation [16].

A third point to be addressed concerns the limitation of the simulations by [11] to axisymmetric dynamics. For displacements in horizontal tubes, this assumption of axisymmetry is equivalent to neglecting gravitational forces. The experiments by [1], on the other hand, suggest that at moderate values of Pe gravity forces related to the different densities of water and glycerin may play an important role. These authors show that the finger of the less viscous fluid can lose its axisymmetry and propagate off-axis in the tube. In addition, they observe a longitudinal splitting phenomenon of the finger in tubes of large diameters, which may be related to gravitational forces. Hence, we will extend the simulations of [11] to three-dimensional flows and account for the presence of gravitational forces.

A final source of the discrepancy between the axisymmetric simulations of [11] and the experimental data of [1] could be the existence of unconventional stresses in regions of high concentration gradients (cf. [17]), along with related divergence effects as described by [18]. This issue will be discussed in more detail below.

The investigation is organized as follows: In Section 2, the physical problem is described, along with the governing equations and their non-dimensionalization. The numerical procedure for solving the three-dimensional Stokes

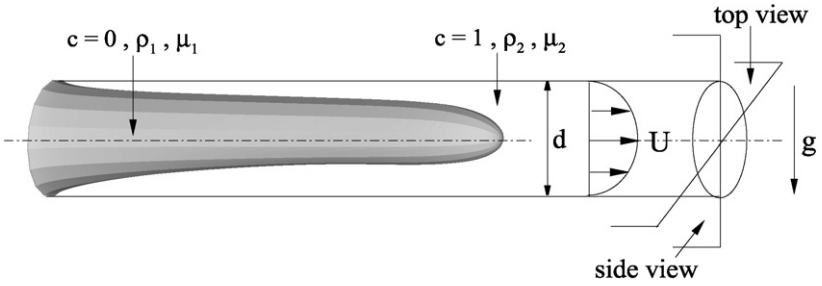

Fig. 1. Sketch of a less viscous fluid 1 displacing a more viscous fluid 2 in a horizontal capillary tube of diameter d. The fluids are fully miscible with each other, and they have different densities. The unperturbed Poiseuille flow far ahead of the finger has a centerline velocity U.

equations in a tube is outlined, and validation results are presented. Section 3 describes the results of axisymmetric simulations for different viscosity–concentration relations and concentration-dependent diffusion coefficients. Section 4 discusses the results of three-dimensional simulations and presents comparisons with experimental data. Section 5 focuses on two-dimensional simulations in the cross-section of the capillary tube and discusses their applicability to three-dimensional displacements. The main conclusions will be presented in Section 6.

2. Physical problem

2.1. Governing equations

We consider the problem of the slow displacement of a more viscous fluid 2 by a less viscous fluid 1 in a horizontal capillary tube of diameter d, cf. Fig. 1. The fluids have different densities and are miscible with each other in all proportions. As our goal is to compare with the experiments of [1] and [12], we assume the Reynolds number is of O(1) or less, so that the motion is governed by the incompressible Stokes equations

$$\nabla \cdot \mathbf{u} = 0, \tag{1}$$

$$\frac{\partial \mathbf{u}}{\partial t} - \nabla \cdot \boldsymbol{\tau}(\mu, \mathbf{u}) + \nabla p = \rho g \mathbf{e_g}, \tag{2}$$

$$\frac{\partial c}{\partial t} + \mathbf{u} \cdot \nabla c = \nabla \cdot (D \nabla c). \tag{3}$$

Here $\mathbf{u}$ denotes the fluid velocity vector, p indicates pressure, c represents the concentration taken to be unity in the displaced fluid and τ is the viscous stress tensor for Newtonian fluids. The density ρ and viscosity μ are assumed to be functions of concentration. The gravitational acceleration g points in the direction of the unit vector $\mathbf{e_g}$, which is perpendicular to the main flow direction. D denotes the molecular diffusion coefficient, which will be assumed constant throughout most of the following investigation. In Section 3.2, however, the influence of a concentration-dependent diffusion coefficient will be evaluated.

In order to close the above set of equations, we must specify both density and viscosity as functions of the concentration c. For most miscible fluid pairs, a linear density–concentration relation represents a good approximation. Hence, we employ

$$\rho = \rho_1 + c(\rho_2 - \rho_1). \tag{4}$$

Combinations of miscible fluids can give rise to qualitatively very different viscosity–concentration relations, ranging from double exponential to non-monotonic relations. Hence, in the past numerical simulations have employed a variety of relations, such as the ones provided by [19,20] and [21]. Following a number of other authors (e.g., [4]), we use an exponential viscosity relation of the form

$$\mu = \mu_2 \mathrm{e}^{R(c-1)} \tag{5}$$

throughout most of the investigation, where the viscosity ratio R is defined as

$$R = \ln \frac{\mu_2}{\mu_1}. \tag{6}$$

The influence of alternative viscosity–concentration functional relations will be investigated in Section 3.1.

To render the governing equations dimensionless, all velocities are normalized by U, which denotes the centerline velocity of the Poiseuille flow far ahead of the displacement front, cf. Fig. 1. All lengths are referred to the tube diameter d, and a characteristic pressure is provided by $\mu_2 U/d$. Density and viscosity are scaled with $\Delta\rho = \rho_2 - \rho_1$ and μ_2, respectively. The dimensionless equations thus read

$$\nabla \cdot \mathbf{u} = 0, \tag{7}$$

$$\frac{\partial \mathbf{u}}{\partial t} + \nabla p = \nabla \cdot \boldsymbol{\tau}(\mu, \mathbf{u}) + Fc\mathbf{e_g}, \tag{8}$$

$$\frac{\partial c}{\partial t} + \mathbf{u} \cdot \nabla c = \frac{1}{Pe}\nabla^2 c, \tag{9}$$

where the Péclet number Pe and the gravity number F are defined as

$$Pe = \frac{U d}{D}, \tag{10}$$

$$F = \frac{g\Delta\rho d^2}{\mu_2 U}. \tag{11}$$

The form of the governing equations for variable diffusion coefficients will be presented in 3.2.

As suggested by Joseph and coauthors [22–24], miscible fluid flows are subject to non-conventional stresses in regions of high concentration gradients (cf. [17]). Furthermore, if the miscible fluids have different densities, they also give rise to a divergent velocity field, as described by [18]. In order to assess if these effects could be responsible for the discrepancies observed between the experiments of [1] and [12] on one hand, and the axisymmetric simulations of [11] on the other, [25] incorporate such Korteweg stresses and divergence effects into axisymmetric simulations, following the formulation of [23]. Their results suggest that Korteweg stresses are not able to explain the observed differences. Moreover, [25] show that for water/glycerin mixtures divergence effects have a negligible effect on the tip velocity. For this reason, we feel that it is justified to neglect these effects in the present numerical investigation.

2.2. Numerical implementation

The system of governing equations (7)–(9) is integrated numerically in cylindrical coordinates. For this purpose, we follow the high-accuracy numerical procedure described in [26] for three-dimensional displacement simulations in capillary tubes. The spatial discretization is based on a mixed spectral element/Fourier spectral scheme [27] with careful treatment of the singularity at the axis. For the temporal discretization a semi-implicit method is applied to the variable viscosity momentum equation, which results in a constant coefficient Helmholtz equation that is solved by a fast diagonalization method. The concentration equation is advanced in time by a mixed implicit-explicit time stepping scheme, i.e., *BDF*2 for the diffusive term and *EX*2 for the convective term [28]. The computation at each time step is performed in the following way: First, the concentration equation is solved using the old velocity and concentration values. Subsequently, the viscosity is updated directly from concentration using (5). Finally, the velocity field is evaluated by solving the momentum and continuity equations together, employing the fractional step method [29].

At the wall of the tube, all velocity components are assumed to vanish, along with the normal derivative of the concentration. At the boundaries far up- and downstream of the mixing region the concentration c equals 0 and 1, respectively, while the velocity profile is assumed to be of Poiseuille type. The initial condition is specified as a one-dimensional error function profile for the concentration,

$$c(r, \theta, z, t = 0) = 0.5 + 0.5 \cdot erf\left(\frac{z}{\delta_0}\right), \tag{12}$$

where δ_0 indicates the initial interface thickness, and an axisymmetric Poiseuille flow for the velocity components. Since the concentration front propagates downstream with a certain tip velocity V_{tip}, some of our simulations employ a reference frame moving with this tip velocity. This allows us to take the simulation farther in time, without discretizing large regions of nearly unperturbed Poiseuille flow. In this moving reference frame, as the upstream boundary catches

up with the trailing sections of the interface, it becomes a mixed inflow/outflow boundary. In this situation, a convective boundary condition for the concentration of the form

$$\frac{\partial c}{\partial t} + V\frac{\partial c}{\partial x} = 0 \tag{13}$$

is applied. Test calculations show that convection velocities V of $O(V_{tip})$ do not result in a loss of accuracy or in numerical instabilities. However, this boundary condition fails to give physical results in some three-dimensional simulations, usually when large velocity gradients occur in the non-axial directions at the upstream boundary. For these cases, we employ the complete computational domain without a moving reference frame. The downstream boundary is always taken to be sufficiently far from the finger tip, so that the concentration can be set to unity. To reduce the computational effort, a parallel implementation is employed for high-resolution calculations. The three-dimensional simulations to be discussed in the following typically employ up to 125 elements in the axial direction, 20 elements in the radial direction, and 32 Fourier modes in the azimuthal direction, with the spectral elements based on either fourth or sixth order Legendre polynomials.

2.3. Validation

As part of the validation process for the present computational code, [26] reproduce the axisymmetric results of [11]. In addition, they consider the case of a density-driven instability at the miscible interface formed by placing a heavier fluid on top of a lighter fluid in a vertical capillary tube. They observe good agreement between the early stages of nonlinear, constant viscosity, three-dimensional simulations and corresponding linear stability results of [30]. This stability work was extended to fluids of different viscosity by [31], which provides us with the opportunity to extend the validation efforts to variable viscosity fluids. Note that in the absence of a net flow, the characteristic velocity U due to buoyancy forces is defined as

$$U = \frac{gd^2\Delta\rho}{\mu_2}. \tag{14}$$

The dimensionless governing equations (7)–(9) remain identical for the vertical tube without net flow, except that they now contain the Rayleigh number

$$Ra = \frac{gd^3\Delta\rho}{D\mu_2} \tag{15}$$

in the place of Pe, while the gravity number F takes the value of unity.

For $Ra = 1.35 \times 10^5$, an initial interface thickness $\delta_0 = 0.2$ and an initial perturbation of $O(10^{-5})$, Fig. 2 shows the maximum value of the axial component of the velocity perturbation as a function of time for the first azimuthal mode,

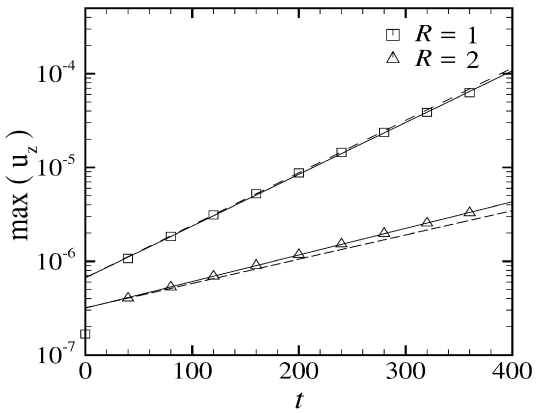

Fig. 2. Maximum axial perturbation velocity component of the first azimuthal mode for $Ra = 1.35 \times 10^5$, $\delta_0 = 0.2$ and viscosity ratios $R = 1$ and 2. The growth rates obtained in the three-dimensional, nonlinear simulations (—) are in good agreement with the corresponding linear stability results (- -) of [31].

for $R = 1$ and 2. We focus on the first azimuthal mode since, for the above parameter values, both the linear stability calculations and the experiments of [13] show this mode to have the largest growth rate. The figure demonstrates that the velocity perturbations grow exponentially, and that the amplification rate decreases with increasing viscosity ratio. The growth rates of the perturbations are seen to be in good quantitative agreement with the corresponding linear stability results. It should be noted that the slight difference arises from the quasisteady state assumption employed in the linear stability calculations.

3. Axisymmetric simulations

As outlined in the introduction, both the experiments of [1] and corresponding axisymmetric simulations by [11] demonstrate the evolution of a quasisteady state for miscible displacements in capillary tubes, provided that *Pe* and R are sufficiently high. This quasisteady state takes the form of a well-defined finger of the less viscous fluid, which propagates along the centerline of the tube, cf. Fig. 3. It is characterized by a front thickness δ that scales as

$$\delta \sim Pe^{-1/2}, \tag{16}$$

and a tip velocity V_{tip}, defined as the propagation velocity of the $c = 0.5$ contour. For the present purpose, we say that a quasisteady state is reached if

$$\left| \frac{dV_{\text{tip}}}{dt} \right| < 0.005. \tag{17}$$

Following the earlier work of [6], [1] and [11] furthermore introduce a diagnostic quantity

$$m = 1 - \frac{0.5}{V_{\text{tip}}}. \tag{18}$$

As explained in the appendix of [12], m is related to the fraction of the more viscous fluid left behind on the wall of the tube. If we assume that the less viscous fluid is injected at a volumetric rate Q, the total volume V_L of less viscous fluid in the tube at time t is equal to $V_L = Qt$. At the same time, the total volume of fluid behind the finger tip is $V_T = \pi d^2 L/4$. Consequently, the volume of more viscous fluid V_M next to the wall behind the finger tip is $V_M = V_T V_L$. m is then defined as

$$m = \frac{V_M}{V_T} = 1 - \frac{V_L}{V_T} = 1 - \frac{Qt}{\pi d^2 L/4}. \tag{19}$$

For incompressible flow in a cylindrical tube, we have $Q = \pi d^2 U_{\text{avg}}/4$ and $V_{\text{tip}} = L/t$. With the present non-dimensionalization $U_{\text{avg}} = 0.5$, so that we obtain (18).

Note that for $V_{\text{tip}} < 1$ ($m < 0.5$), the finger tip moves more slowly than the centerline velocity of the Poiseuille flow ahead of it. For this situation, [1] and [11] show that the less viscous fluid diffusively leaks from the finger tip into the more viscous fluid ahead of it, so that a quasisteady tip propagation is not possible. This point will be discussed in more detail below.

For $Pe > \mathrm{O}(10^4)$ the numerical simulations of [11] showed good agreement with the corresponding experiments of [1] regarding V_{tip}. For $Pe < \mathrm{O}(10^4)$, on the other hand, the quasisteady front velocity in the experiments decreased noticeably with *Pe*, a fact that was confirmed more recently in the silicone oil experiments of [12], whereas it remained nearly constant in the axisymmetric simulations. In the following, we will discuss the results of additional axisymmetric simulations ($F = 0$), in order to explore if either the specific properties of the viscosity–concentration relation, or the dependence of the diffusion coefficient on the local concentration value can account for these discrepancies.

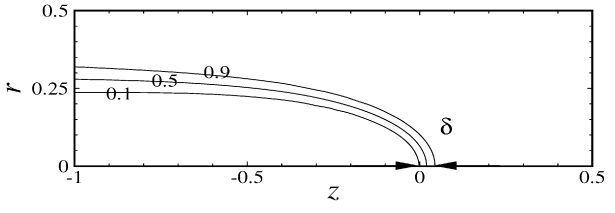

Fig. 3. Quasisteady finger front for $R = 2.3$ and $Pe = 2000$. Shown are the concentration contours $c = 0.1$, 0.5 and 0.9 at time $t = 2.5$. δ denotes the front thickness.

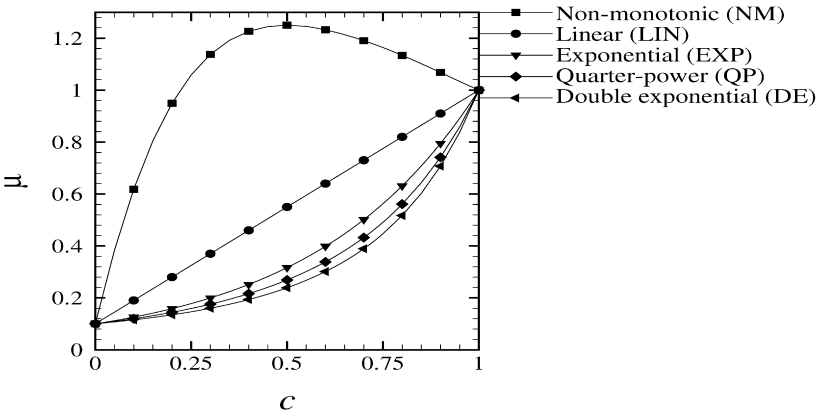

Fig. 4. Nondimensional μ, c-relations in the interval $0 \leqslant c \leqslant 1$ for various functional relations and $R = 2.3$.

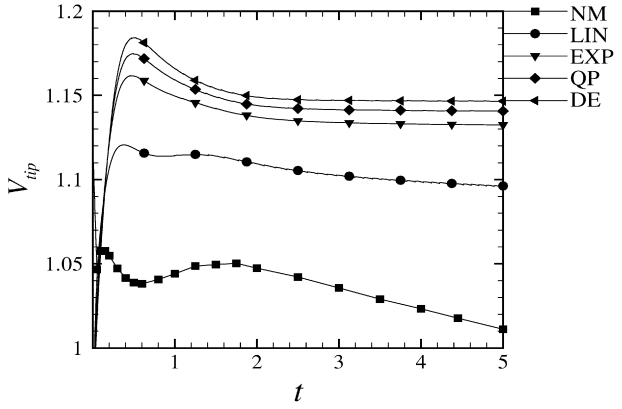

Fig. 5. The tip velocity V_{tip} as a function of time for $R = 2.3$, $Pe = 2000$ and different μ, c-relations. The double exponential relation yields the highest quasisteady V_{tip} value, while non-monotonic and linear viscosity relations do not result in a steady state at this value of the Péclet number.

3.1. Influence of the μ, c-relation

In miscible fluid mixtures, the dependence of the viscosity on the concentration can take different functional forms. Hence a variety of μ, c-relations have been employed in the literature. [32] assume the viscosity to be a linear function of concentration in his linear stability calculations. Alternatively, [11] use an exponential viscosity relation, which closely resembles the 'quarter-power mixing rule' frequently employed by petroleum engineers [33,34,20]. Interestingly, some fluid mixtures can even display a non-monotonic variation of viscosity with concentration [21,35].

Fig. 4 displays representative non-dimensional forms for various μ, c-relations. The formulation of the non-monotonic viscosity relation follows the approach outlined in [21]. Here, the viscosity reaches a maximum value of $1.25\mu_2$ for $c = 0.5$. The double exponential viscosity relation suggested by [1], based on their experimental measurements, is implemented as

$$\mu = \mathrm{e}^{R\left(\frac{\mathrm{e}^{c}-\mathrm{e}}{\mathrm{e}-1}\right)}. \tag{20}$$

Fig. 5 shows the results of axisymmetric simulations ($F = 0$) for $R = 2.3$, $Pe = 2000$, and the above μ, c-relations. For the non-monotonic and linear relations, the tip velocity does not reach a quasisteady state at this value of Pe. On the other hand, for the remaining μ, c-relations V_{tip} approaches a constant value. [11] had shown that for a quasisteady state to be achieved, generally a Pe-value on the order of 10^3 is necessary. This quasisteady state then lasts for a time of $\mathrm{O}(Pe)$. For Pe-values below $\mathrm{O}(10^3)$, a quasisteady state usually does not form, and Taylor dispersion becomes dominant immediately. The quasisteady tip velocity increases with the steepness of the relation. Fig. 6 shows the fraction m as a function of Pe for $R = 2.3$ and different μ, c-relations. There are noticeable differences at low Pe,

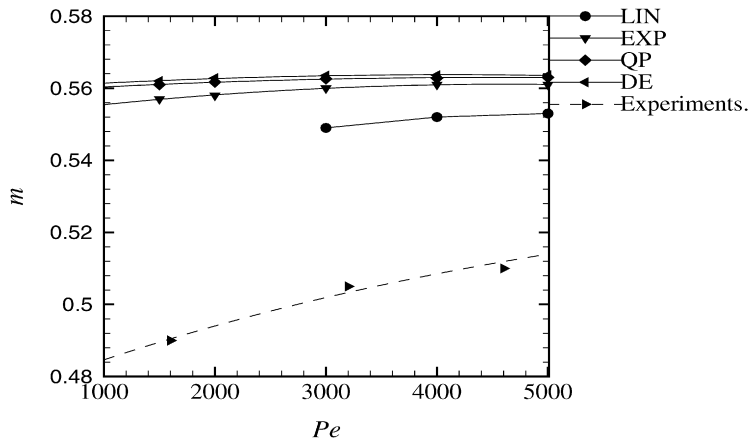

Fig. 6. The fraction m as a function of Pe, for different μ, c-relations and $R = 2.3$. Differences between the results for the various μ, c-relations are noticeable for moderate Pe. However, these effects are too small to account for the discrepancies between the computational results of [11], and the corresponding experimental data of [12] (- -).

where the interfacial thickness is sufficiently large for the details of the μ, c-relation to be felt. As Pe increases, the interface thins and the details of the relation become less influential. Note that all of the computational curves lie considerably above the experimental data of [12]. In summary, these observations indicate that the precise form of the μ, c-relation has a limited influence on the quasisteady tip velocity at $Pe < \mathrm{O}(10^4)$. However, this effect is too small to explain the discrepancies between the axisymmetric simulations by [11] and the corresponding experiments by [1] and [12]. For the remainder of the present investigation, we will employ the exponential μ, c-relation.

3.2. Influence of a concentration-dependent diffusion coefficient

The measurements of [1] indicate that for the fluid pair of water and glycerin the diffusion coefficient varies strongly with concentration, cf. also the measurements of [15]. It has already been demonstrated that this dependence can strongly affect the linear dynamics of miscible interfaces, e.g. the linear stability analyses of [36] and [37]. Here we will investigate its effect on the *nonlinear* quasisteady finger, in order to assess if it is sufficiently strong to explain the discrepancies between the experimental data of [1] and the corresponding simulation data of [11].

For different fluid combinations, the dependence of the diffusion coefficient on the concentration can take different forms. Often it is well approximated by the generalized Stokes–Einstein relation (cf. [16])

$$D \cdot \mu = const., \tag{21}$$

which we will assume to hold in the following. For the formulation of the governing equations in the presence of a variable diffusion coefficient we follow the approach outlined in [37]. Eqs. (5) and (21) yield for the diffusion coefficient

$$D = D_1 \mathrm{e}^{-Rc}, \tag{22}$$

where D_1 denotes the diffusion coefficient of an infinitesimally small amount of fluid 2 in pure fluid 1. The dimensional diffusion coefficient is normalized by its average value D^*

$$D^* = \int_0^1 D\,dc = \frac{D_1(1-\mathrm{e}^{-R})}{R}, \tag{23}$$

so that a meaningful comparison can be made with calculations assuming a constant diffusion coefficient. This implies that with an increasing value of R the diffusion coefficient varies over a larger range, while its average value remains unchanged. Definition (10) of Pe is modified to

$$Pe = \frac{U d}{D^*}. \tag{24}$$

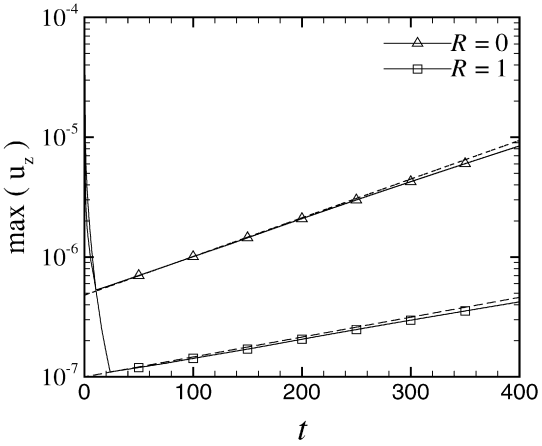

Fig. 7. Maximum of the axial perturbation velocity component for $Ra = 1.35 \times 10^5$, $\delta_0 = 0.2$ and viscosity ratios $R = 0$ and 1. The growth rates from nonlinear axisymmetric simulations (—) are in good agreement with the corresponding linear stability results (- -) of [37].

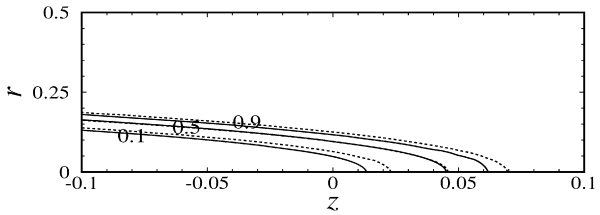

Fig. 8. Concentration contours $c = 0.1$, 0.5 and 0.9 at $t = 2.5$ for quasisteady fingers with $R = 2.3$ and $Pe = 2000$: variable (—) and constant diffusion (- -) coefficients.

When treating the convection–diffusion equation (9) numerically in the presence of a variable diffusion coefficient, we adopt the same approach as for the variable viscosity momentum equation, since it allows for an implicit treatment of the diffusion operator even though D changes spatially and temporally. This computational approach is validated by a comparison of nonlinear simulation data with linear stability results for density-driven instabilities in vertical capillary tubes, cf. [37]. For $Ra = 1.35 \times 10^5$, an initial interface thickness $\delta_0 = 0.2$ and an initial perturbation of $O(10^{-5})$, Fig. 7 shows the maximum axial perturbation velocity component as a function of time for $R = 0$ and 1. For both viscosity ratios, good agreement is observed.

For $Pe = 2000$ and $R = 2.3$, Fig. 8 compares the concentration contours of quasisteady fingers for constant and variable D simulations. For ease of comparison, the variable D results have been shifted in the streamwise direction, so that the $c = 0.5$ contours cross the centerline at identical locations. For the variable diffusion calculations, D varies by a factor of $e^{2.3} \sim O(10)$ across the finger front. Due to the stronger diffusion on the inside of the finger, the $c = 0.1$ contour lags behind its counterpart for constant D, while the $c = 0.9$ also lags behind its constant D counterpart, but now due to the locally reduced diffusion on the outside of the finger. However, the overall finger shape is quite similar for both cases.

Fig. 9(a) indicates that the tip moves more slowly for a variable D, as compared to the constant D case. This effect increases with R as a result of the larger variation of D across the finger front. In Fig. 9(b) the fraction m is plotted as a function of Pe for constant and variable D, respectively, at $R = 2.3$. For $Pe > 2000$ the interface is thin enough for the influence of variations in D to become negligible. Below $Pe = 2000$, however, a concentration dependent diffusion coefficient is seen to lower the tip velocity. Here the interface is sufficiently thick for the details of the diffusion profile to be felt. The trend of a lower tip velocity shifts the computational data of [11] towards the experimental data of [12], although the magnitude of the effect is too small to account for the discrepancy by itself.

In summary, the axisymmetric simulation results indicate that a less steep μ, c-relation and/or a concentration dependent diffusion coefficient can lower the tip velocity, and hence m, somewhat. However, these effects are relatively small, so that we now turn towards three-dimensional dynamics as the possible reason for the discrepancies between

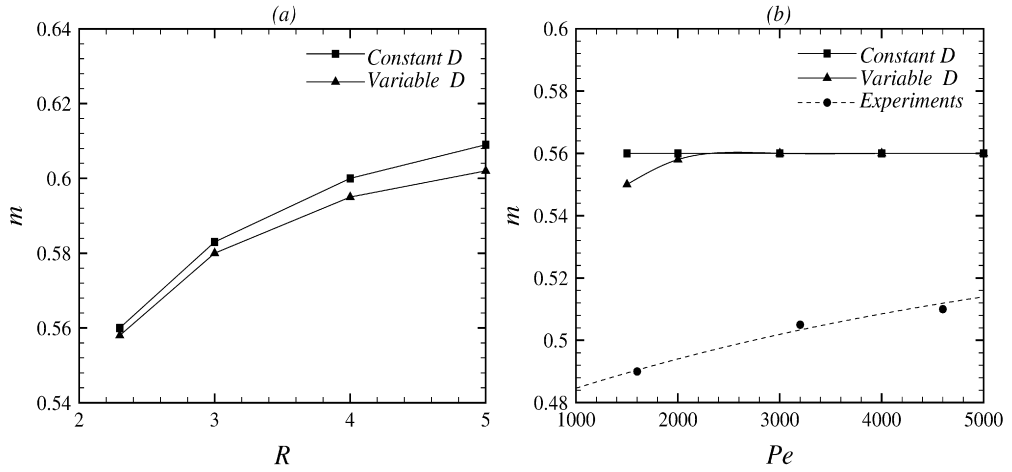

Fig. 9. The fraction m as a function of (a) R at $Pe = 2000$, (b) Pe with $R = 2.3$ for variable and constant diffusion coefficients, respectively. In (a) the variable diffusion coefficient is seen to lower the tip velocity. This effect is more pronounced for larger R. In (b) the experimental values of [12] are shown by dashed lines. A variable diffusion coefficient lowers the tip velocity somewhat at moderate Pe, although the effect is too small to fully explain the discrepancy between experimental and computational data.

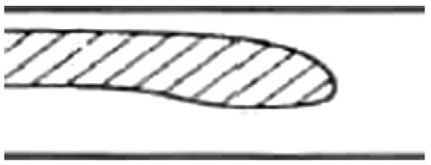

Fig. 10. Qualitative shape of a three-dimensional finger (side view) observed in the experiments of [1] (the sketch is reproduced from their work).

the earlier experimental and computational data. For the remainder of this investigation, we will assume the diffusion coefficient to be constant.

4. Three-dimensional simulations

The experiments of [1] demonstrate that as the finger of the less viscous water–glycerin mixture channels through the more viscous pure glycerin, it rises within the narrow confines of the horizontal tube and develops a three-dimensional shape, cf. Fig. 10. Due to the small cross-section of the capillary tube, the authors do not obtain quantitative information about the finger shape. For tubes of larger diameters, [1] report that a longitudinal splitting phenomenon can develop which cuts the finger into two parts. Unfortunately, not even an approximate parameter combination for the appearance of this instability is provided.

Fig. 11 displays side views of the evolving computational finger shape for $Pe = 2000$, $R = 2.3$ and $F = 10$. The $c = 0.1$, 0.5 and 0.9 contours indicate that the tip of the finger remains close to the axis as it propagates along the tube. Its trailing sections rise as a result of gravitational forces, so that most of the finger is situated in the upper half of the capillary tube. The qualitative shape of the finger agrees well with the experimental observations, cf. Fig. 10. For these three-dimensional finger shapes, we can define the tip velocity V_{tip} as the velocity of the most advanced point of the $c = 0.5$ contour.

The accompanying streamline pattern in a reference frame moving with the tip velocity is displayed in Fig. 12(a) (side view) and (b) (top view). The stagnation point at the finger tip is raised slightly above the axis, while the top view remains similar to the axisymmetric case for $F = 0$, cf. Fig. 13. These streamline patterns indicate that at the tip most of the more viscous fluid moves underneath the finger. Those portions of the viscous fluid that initially enter the gap between the top of the finger and the upper wall are subsequently squeezed out of this gap by the rising finger sections far behind the tip. In this way, the more viscous fluid acquires an azimuthal velocity component that transports it downward around the outside of the finger, while the fluid within the finger rises. This picture is confirmed by the cross-sectional streamline patterns at different axial locations in Fig. 14.

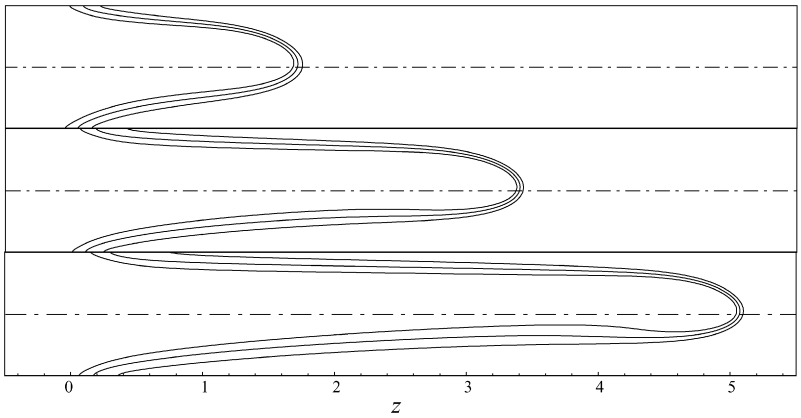

Fig. 11. Concentration contours (side view) at $t = 1.5$, 3 and 4.5, for $R = 2.3$, $Pe = 2000$ and $F = 10$. Due to gravitational forces, the trailing sections of the finger rise, so that it is positioned mostly in the upper part of the capillary tube.

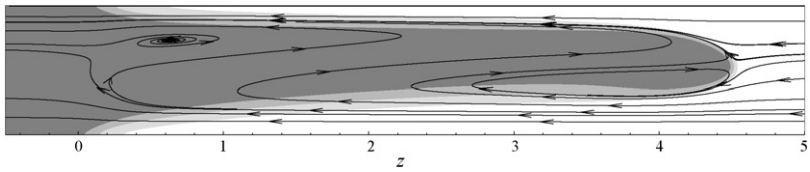

(a) side view

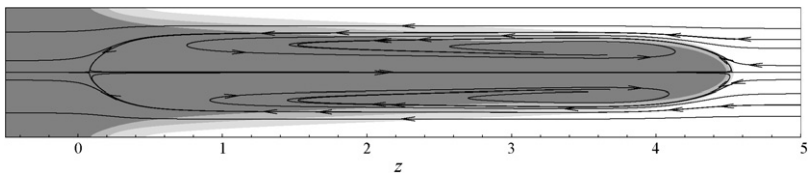

(b) top view

Fig. 12. Streamlines of the in-plane velocity components at $t = 4$ for $R = 2.3$, $Pe = 2000$ and $F = 10$. The grey shading indicates the concentration level of the less viscous fluid. The side view shows that the stagnation point at the tip is raised above the axis.

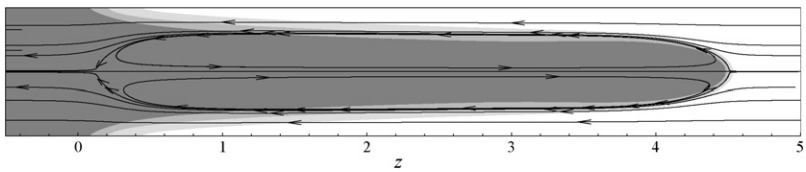

Fig. 13. Axisymmetric streamline pattern at $t = 4$ for $R = 2.3$, $Pe = 2000$ and $F = 0$.

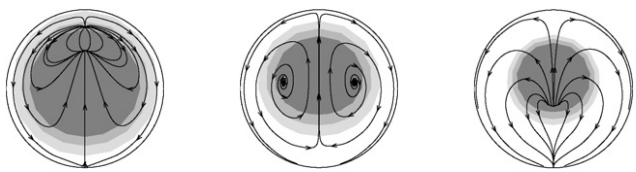

(a) $z = 0.5$ (b) $z = 2.5$ (c) $z = 4$

Fig. 14. Cross-sectional streamline patterns at various axial locations (cf. Fig. 12) at $t = 4$ for $R = 2.3$, $Pe = 2000$ and $F = 10$.

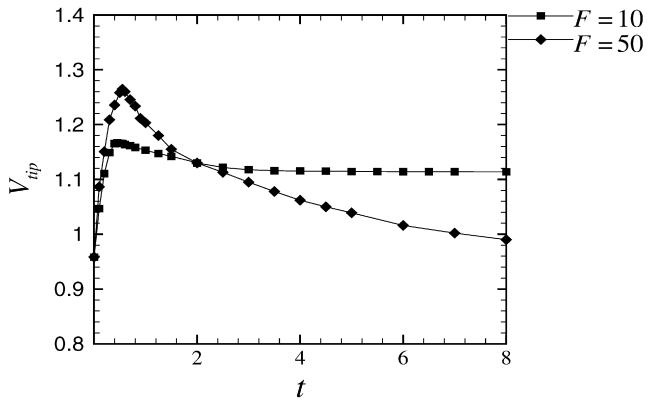

Fig. 15. Tip velocity V_{tip} as a function of time for $R = 2.3$, $Pe = 2000$ and $F = 10$ and 50, respectively. While for $F = 10$ a quasisteady state is reached, this is not the case for $F = 50$.

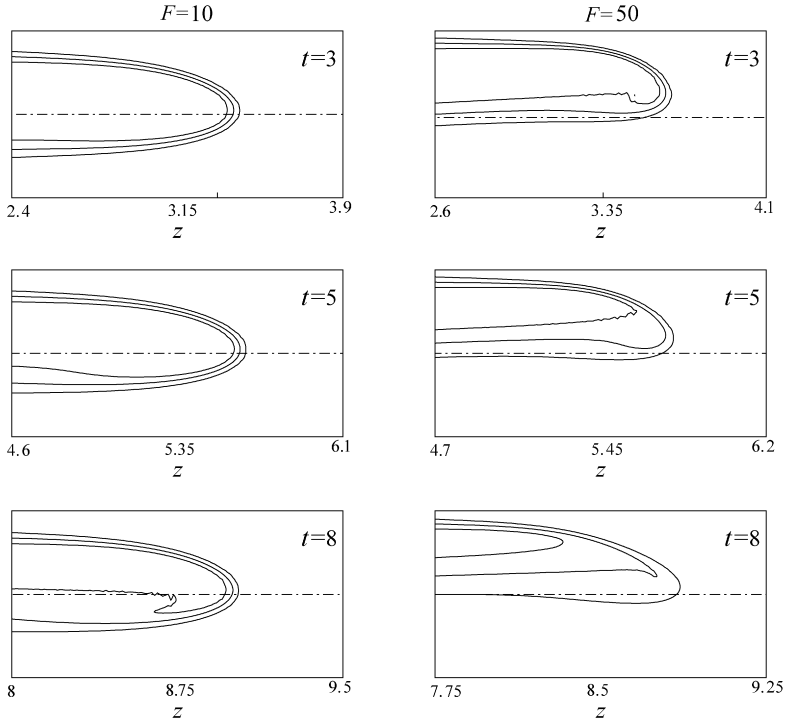

Fig. 16. Concentration contours $c = 0.1$, 0.5 and 0.9 in the tip region (side view) for $R = 2.3$, $Pe = 2000$ and $F = 10$ and 50, respectively, at various times.

Fig. 15 indicates that for small F the finger of the less viscous fluid reaches a quasisteady state according to (17). On the other hand, for large values of the gravity parameter F a quasisteady state is not achieved. This is confirmed by Fig. 16, which shows concentration contours as a function of time for $R = 2.3$, $Pe = 2000$ and $F = 10$ and 50, respectively. For $F = 10$ the contours near the tip show very little change in the time interval $3 < t < 8$, although some distance behind the tip the streamline pattern does vary with time, cf. also the cross-sectional contours in Fig. 17. This indicates that even those flows that do exhibit a quasisteady tip velocity according to criterion (17), are not truly independent of time. For $F = 50$ the concentration contours at the tip change continuously with time from the very beginning, so that a quasisteady state does not develop. The cross-sectional concentration contours in Fig. 17 indicate the development of a 'dimple' on the lower side of the finger, about one diameter behind the tip. This dimple can also be seen clearly in the perspective view of Fig. 18. We speculate that this dimple may possibly be a precursor to

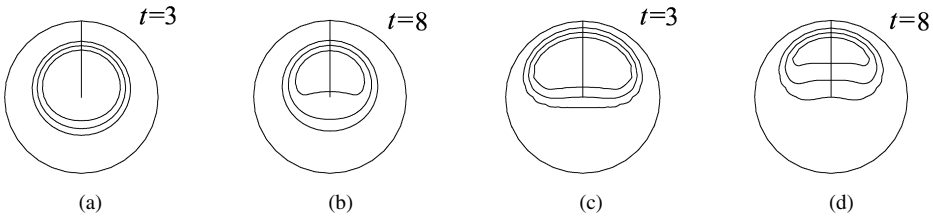

Fig. 17. Concentration contours $c = 0.1$, 0.5 and 0.9 in the cross-section one diameter behind the tip for $F = 10$ (a), (b) and $F = 50$ (c), (d), respectively, at $R = 2.3$ and $Pe = 2000$. The formation of a dimple is visible on the lower side of the finger for $F = 50$.

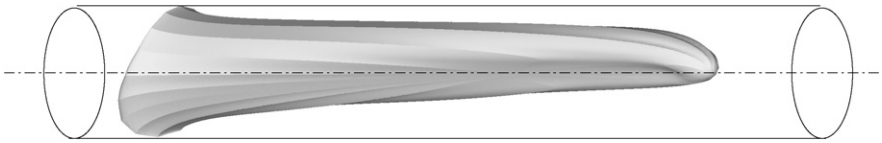

Fig. 18. Perspective view of the $c = 0.2$ concentration contour for $R = 2.3$, $Pe = 2000$ and $F = 30$ at time $t = 4$. The dimple is visible on the lower side of the finger, shortly behind the tip.

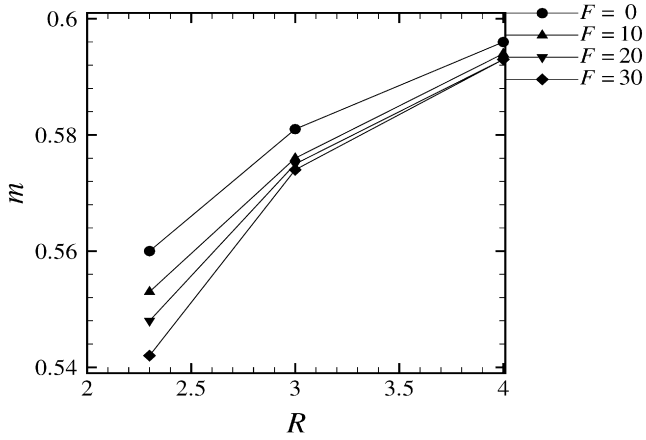

Fig. 19. The fraction m as a function of F for $Pe = 2000$ and various R. The influence of gravity decreases with increasing R.

a longitudinal splitting event originating at the finger tip, although computational limitations did not allow us to carry the simulations to sufficiently long times to explore this hypothesis.

4.1. Influence of R and Pe

Fig. 19 shows the fraction m as a function of R for $Pe = 2000$ and various F. With increasing R, viscous forces become dominant, so that the relative importance of gravitational forces decreases. At large R, we find that there is a clear difference between $F = 0$ and $F \neq 0$, although the precise magnitude of F does not have a significant effect on m. This reflects the fact that even small gravitational forces are able to prevent the flow from being axisymmetric, and to cause the trailing finger sections to rise to the top wall. The exact value of F, on the other hand, is not very influential in determining the detailed features of the quasisteady flow. In general, for a fixed R the tip velocity decreases with increasing F. In order to explain this observation, we define d_w as the distance of the $c = 0.5$ contour from the upper wall, one diameter behind the tip in the symmetry plane. Fig. 20 shows d_w as a function of F for $Pe = 2000$ and $R = 2.3$. For increasing F the finger is seen to move closer to the wall, which reduces its tip velocity.

Fig. 21 shows the fraction m as function of Pe, for $R = 2.3$ and various values of F. For all Pe, m is seen to decrease with increasing F. Moreover, gravitational effects lower m more significantly at low Pe, which is consistent with the experimental observations of [1] and [12]. For a fixed combination of Pe and R, a steep concentration profile

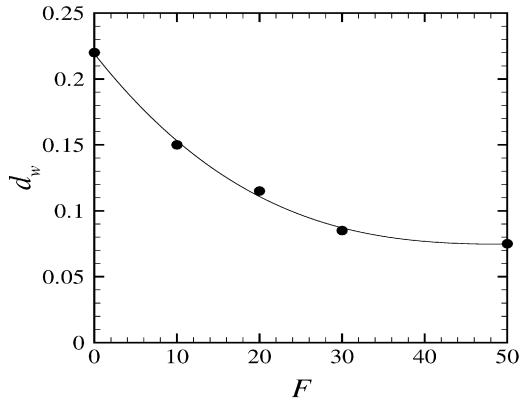

Fig. 20. The distance d_w between the upper wall and the $c = 0.5$ contour one diameter behind the finger tip at $t = 4$, for $Pe = 2000$, $R = 2.3$ and various values of F. With increasing F, the finger moves closer to the upper wall, which reduces its propagation velocity.

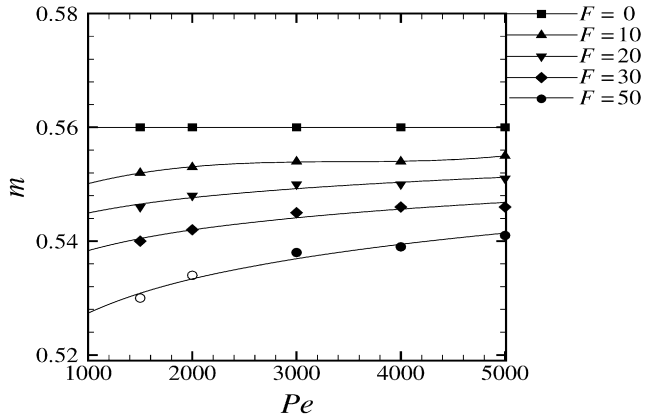

Fig. 21. The fraction m as a function of Pe for $R = 2.3$ and various F. Gravitational effects uniformly reduce the tip velocity. This effect is more pronounced at lower Pe. Open symbols correspond to cases when a quasisteady state according to Eq. (17) is not achieved.

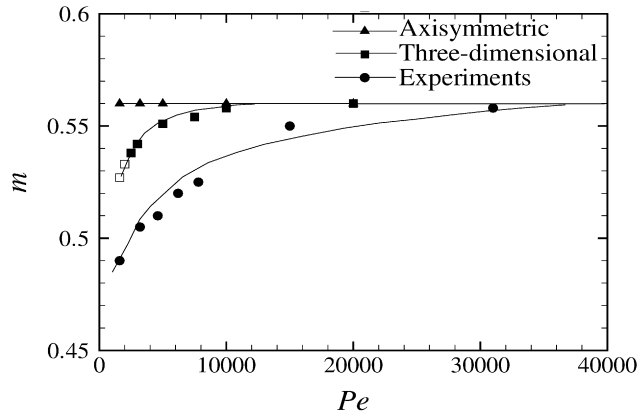

Fig. 22. The fraction m as function of Pe for $R = 2.3$. In each three-dimensional simulation, the F value was chosen to match the experiments of [12] (- -). Note that the open symbols correspond to cases where a quasisteady state is not fully reached in the simulations. The three-dimensional simulation results capture the experimentally observed trend, although the magnitude of the effect is less pronounced in the simulations. At the lowest values of Pe, three-dimensional effects are seen to account for about half the discrepancy between the experimental data and the earlier, axisymmetric simulations of [11].

Table 1
The gravity parameter F as a function of Pe at $R = 2.3$, for the $d = 2mm$ capillary tube employed in the experiments of [12]

Pe	1.6×10^3	2×10^3	2.5×10^3	3×10^3	5×10^3	7.5×10^3	1×10^4	2×10^4
F	66	53	42	35	21	14	10	5

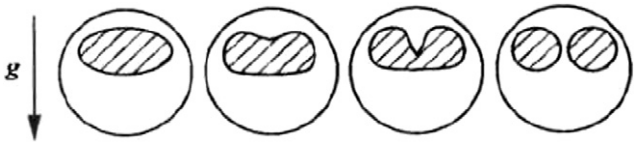

Fig. 23. For some parameter combinations, [1] observe a longitudinal splitting of the finger. They speculate that a gravitational instability, triggered by the heavier fluid above the finger, may be responsible, as indicated in this sketch from their work.

cannot be maintained beyond a certain value of F, so that a quasisteady state is not attained. This threshold value of F increases with Pe.

4.2. Comparison with experiments

For $R = 2.3$, Fig. 22 compares the three-dimensional simulation results for m with the experimental data of [12]. The axisymmetric simulation data of [11] are included as well. In the three-dimensional simulations, the value of F at each Pe was chosen to correspond to the experimental parameters, cf. Table 1. The results indicate that the three-dimensional simulations capture the experimentally observed trend of m at low Pe. However, the slowdown effect is not as pronounced in the simulations, and at the lowest Pe accounts for only about half the discrepancy between the experimental data reported by [1] and [12], and the axisymmetric simulations of [11]. We conclude that, while the simulations do not show very close agreement with the experimental data, they demonstrate that three-dimensionality triggered by gravitational forces does provide a slowdown of the correct order of magnitude.

Regarding the remaining discrepancy, we wish to comment also on the experimental data for the quasisteady tip velocity at the lowest Pe-values. For $Pe = 1600$ [12] report a value of $m \approx 0.49$. This value indicates that the finger tip moves more slowly than the centerline Poiseuille flow velocity ahead of it. At the same time, [1,11] and [12] show that a value $m < 0.5$ leads to a diffusive leakage of the less viscous fluid into the more viscous fluid ahead of it, so that a quasisteady state cannot exist. Hence it cannot be ruled out that the lowest experimentally reported tip velocity data do not reflect truly quasisteady states. This might partly explain the discrepancy with the three-dimensional simulation data.

Furthermore, note that the axisymmetric simulations with concentration dependent diffusion coefficient discussed in Section 3.2 indicate that with a variable D the tip velocity decreases further at low Pe. Hence, we would expect the comparison of experimental and simulation data to improve further if the concentration dependence of D were incorporated in the three-dimensional simulations.

5. Two-dimensional simulations in the cross-section of the capillary tube

In some of their experiments, [1] observe a splitting phenomenon that divides the finger longitudinally. They speculate that this may be triggered by a gravitational instability, as sketched in Fig. 23, which is reproduced from their work. The authors provide estimates for the wavelength and time scale of this instability. However, they do not provide any information regarding the parameter combination when the splitting occurs, or concerning its spatio-temporal development.

Within the present investigation, computational constraints limited three-dimensional simulations to the parameter range $10^3 \leqslant Pe \leqslant 10^4$, $1 \leqslant R \leqslant 4$, $0 \leqslant F \leqslant 50$ and $0 \leqslant t \leqslant 15$. The estimate by [1] for the characteristic time scale of the gravitational instability translates into

$$t = \left(\frac{Pe^{0.5}}{F} \right)^{2/3} \tag{25}$$

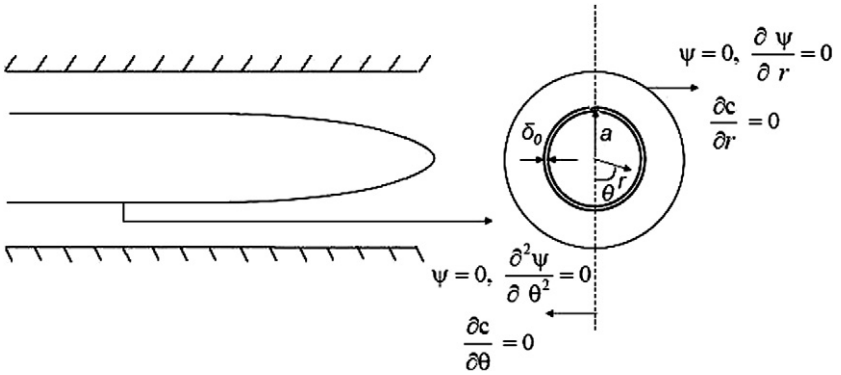

Fig. 24. The computational domain and boundary conditions employed for two-dimensional simulations in cross-sections of the tube.

for the present non-dimensionalization. For the representative values of $Pe = 4000$ and $F = 25$, we obtain the relatively short dimensionless time of $t = 1.64$. Even though our simulations generally extended over substantially longer time intervals, we did not observe any splitting events similar to the sketch in 23. Note that in the absence of experimental information regarding the parameter combination where the splitting was observed, we could only do a limited search within the multidimensional parameter space, especially in light of the considerable computational expense of the three-dimensional simulations. In order to shed additional light on the splitting issue, we conducted a series of simulations for two-dimensional cross-sections of the finger. The rationale behind this approach is that, beyond some distance behind the tip, the finger shape changes only slowly along the tube. Consequently, three-dimensional effects should be relatively unimportant for the further evolution of these trailing finger sections. For the cross-sectional simulations, the dimensionless Stokes equations are solved in the (r, θ)-plane, cf. Fig. 24. The streamfunction formulation is employed, so that the pressure variable is eliminated and the continuity equation is satisfied identically. The governing equations have the form

$$\begin{aligned}
&\psi_{rrrr} + \psi_{rr\theta\theta}\left(\frac{2}{r^2}\right) + \psi_{\theta\theta\theta\theta}\left(\frac{1}{r^4}\right) + \psi_{rrr}\left(\frac{2}{r} + 2R\frac{\partial c}{\partial r}\right)\\
&\quad + \psi_{\theta\theta\theta}\left(\frac{2R}{r^4}\frac{\partial c}{\partial \theta}\right) + \psi_{r\theta\theta}\left(\frac{2R}{r^2}\frac{\partial c}{\partial r} - \frac{2}{r^3}\right) + \psi_{rr\theta}\left(\frac{2R}{r^2}\frac{\partial c}{\partial \theta}\right)\\
&\quad + \psi_{rr}\left(\frac{R}{r}\frac{\partial c}{\partial r} - \frac{1}{r^2} + R^2\frac{\partial^2 c}{\partial^2 r} - \frac{R^2}{r^2}\frac{\partial^2 c}{\partial^2 \theta}\right) + \psi_{r\theta}\left(\frac{4R^2}{r^2}\frac{\partial^2 c}{\partial\theta\,\partial r} - \frac{2R}{r^3}\frac{\partial c}{\partial th}\right)\\
&\quad + \psi_{\theta\theta}\left(\frac{4}{r^4} - \frac{3R}{r^3}\frac{\partial c}{\partial r} - \frac{R^2}{r^2}\frac{\partial^2 c}{\partial^2 r} + \frac{R^2}{r^4}\frac{\partial^2 c}{\partial^2 \theta}\right) + \psi_{\theta}\left(\frac{R}{r^4}\frac{\partial c}{\partial \theta} - \frac{4R^2}{r^2}\frac{\partial^2 c}{\partial\theta\,\partial r}\right)\\
&\quad + \psi_{r}\left(\frac{1}{r^3} - \frac{R}{r^2}\frac{\partial c}{\partial r} - \frac{R^2}{r}\frac{\partial^2 c}{\partial^2 r} + \frac{R^2}{r^3}\frac{\partial^2 c}{\partial^2 \theta}\right) = G(r,\theta),\\
&\frac{\partial c}{\partial t} + \mathbf{u}\cdot\nabla c = \frac{1}{Ra}\nabla^2 c,
\end{aligned} \tag{26}$$

where the streamfunction ψ is defined, in the usual way, as

$$v_r = \frac{1}{r}\frac{\partial \psi}{\partial \theta}, \qquad v_\theta = -\frac{\partial \psi}{\partial r},$$

the forcing function G is

$$G(r,\theta) = -\frac{F}{r\mu}\left(r\sin(\theta)\frac{\partial c}{\partial r} + \cos(\theta)\frac{\partial c}{\partial \theta}\right),$$

and the Rayleigh number Ra is defined as

$$Ra = \frac{g d^3 \Delta\rho}{D\mu_2}. \tag{27}$$

5.1. Numerical implementation

Fig. 24 shows the two-dimensional computational domain along with the imposed boundary conditions. Only the half $\theta \in [0, \pi]$ of the cross-section is employed in the simulations, due to the inherent symmetry of the problem. Symmetry conditions are implemented for the streamfunction and concentration at $\theta = 0$ and $\theta = \pi$. To avoid the singularity at $r = 0$ in the concentration equation, we employ a staggered grid so that only streamfunction values are required on the axis. For solving the streamfunction equation (26) along with the species conservation equation, we adapt the computational approach outlined in [38]. Second order finite differences are employed for the spatial discretization of the streamfunction derivatives. The discretized fourth order streamfunction equation is solved by the sparse direct linear solver implemented in the software package UMFPACK [39]. For the concentration equation, compact finite differences [40] of up to sixth order in the interior of the domain and fourth order at the boundaries are employed. The time integration is fully explicit and utilizes a third order low-storage Runge–Kutta [41] procedure. Initial conditions are prescribed as

$$\psi(r, \theta, t = 0) = 0, \tag{28}$$

and

$$c(r, \theta, t = 0) = 0.5 + 0.5 \cdot erf\left(\frac{r - a}{\delta_0}\right), \tag{29}$$

where δ_0 indicates the thickness of the interface. The above condition specifies a circular drop with radius a placed at $r = 0$. The influence of different initial shapes will be investigated below as well.

For validation purposes we compared the simulation results with a different computational procedure that we had developed earlier, based on the vorticity-streamfunction formulation of the momentum equation. This approach, which employs a Fourier scheme in the azimuthal direction and compact finite differences in the radial direction, involves iterations between the vorticity and streamfunction equations at every time step. However, it fails to converge for $R > 2.5$, so that it was not employed for the parametric study. Additional validation information is presented in Section 5.2 in the form of comparisons with three-dimensional simulations.

5.2. Comparison between two- and three-dimensional simulations

In order to compare two-dimensional calculations in a cross-section with three-dimensional simulation results, we remind the reader that

$$Ra = Pe \times F, \tag{30}$$

$$t_{2D} = t_{3D} \times F, \tag{31}$$

where t_{2D} and t_{3D} represent the dimensionless times in two- and three-dimensional simulations, respectively. As a first step, we need to clarify under which circumstances three-dimensional flow effects in the trailing finger sections are small, so that two-dimensional simulations of cross-sectional flows can provide meaningful information. Towards this end, it is helpful to inspect streamwise profiles of the mean concentration averaged over the cross-section

$$c_m(z) = \frac{4}{\pi} \int_0^{2\pi} \int_0^{0.5} c(r, \theta, z) r \, dr \, d\theta. \tag{32}$$

Fig. 25 shows the temporal evolution of $c_m(z)$ for $Pe = 4 \times 10^3$, $F = 25$, and $R = 2.3$ and 4, respectively. For $R = 2.3$, the value of c_m is seen to change with time at each z-location. This indicates that the effective finger diameter at each location grows with time, which can only happen as a result of three-dimensional flow effects. On the other hand, for $R = 4$, c_m remains approximately constant in time for z-locations sufficiently far behind the tip, which reflects a predominantly two-dimensional flow field. Under these circumstances, we can expect to obtain meaningful information from two-dimensional simulations of the cross-sectional flow.

For the case of Figs. 25(b), 26(a) depicts concentration contours in the $z = 2.5$ cross-section at three different times. We then carried out a two-dimensional simulation in the $z = 2.5$ cross-section, with the contours of the first

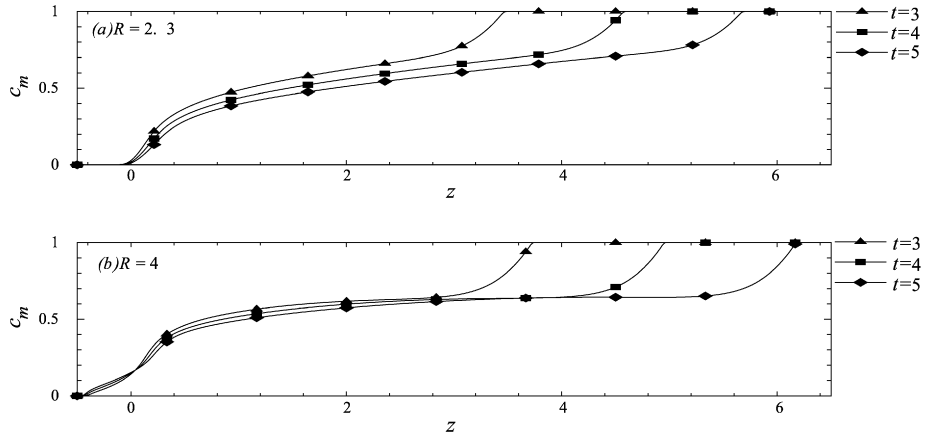

Fig. 25. Cross-sectionally averaged mean concentration c_m as function of the axial location for different times: $Pe = 4 \times 10^3$, $F = 25$ and $R = 2.3$ (a) and $R = 4$ (b). For $R = 4$ the values of c_m remain constant in time sufficiently far behind the tip, which indicates that the flow is predominantly two-dimensional.

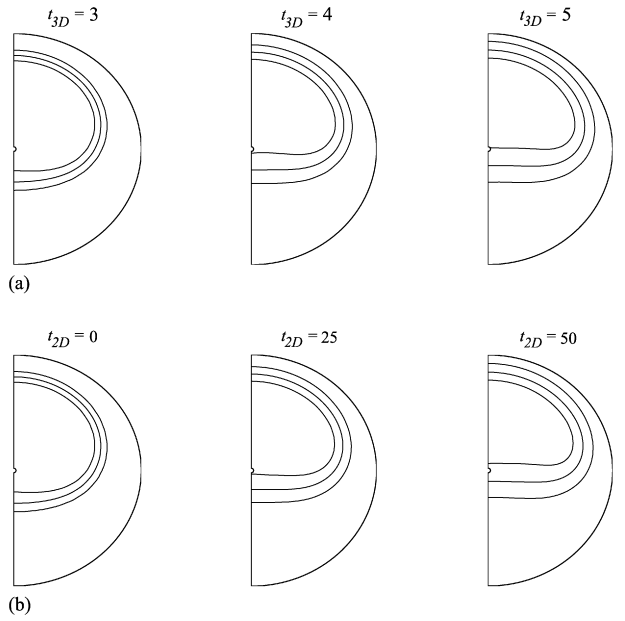

Fig. 26. (a) Three-dimensional simulation results: concentration contours in the $z = 2.5$ cross-section for $Pe = 4 \times 10^3$, $R = 4$ and $F = 25$. (b) Two-dimensional simulation results at corresponding times for $Ra = 10^5$ and $R = 4$: cross-sectional concentration contours, with the initial condition taken from the three-dimensional calculations at $z = 2.5$ and $t_{3D} = 3$. The good agreement between the two sets of results indicates that for these parameter values the flow in the trailing sections is dominated by two-dimensional effects.

frame of Fig. 26(a) specified as initial condition. The parameters of this cross-sectional simulation are set to $Ra = 10^5$ and $R = 4$, which corresponds to the values of $Pe = 4 \times 10^3$, $R = 4$ and $F = 25$ in the three-dimensional simulation. The times of frames two and three of Fig. 26(b) are chosen to correspond to frames two and three of Fig. 26(a). The good agreement between the two simulations confirms the approximately two-dimensional nature of the flow in the trailing sections of the finger, which enables us to obtain information on the long-term evolution of the finger from cross-sectional simulations. Along these lines, Fig. 27 shows the shape of the finger at $t_{2D} = 100$, 200 and 300, or correspondingly at $t_{3D} = 7$, 11 and 15. The concentration contours indicate that with increasing time the finger reaches the upper wall, as diffusion effects result in the thickening of the interface between the fluids. Note that a gravitational instability does not develop. The above comparison confirms the relevance of two-dimensional simulations in the

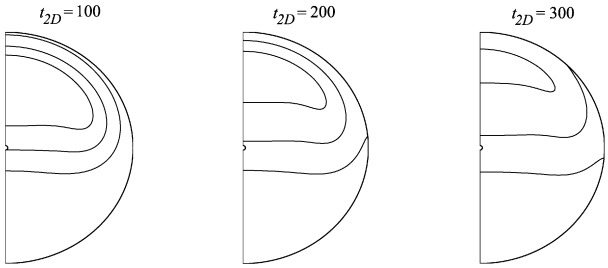

Fig. 27. Long-term evolution of the contours shown in Fig. 26. A gravitational instability does not develop.

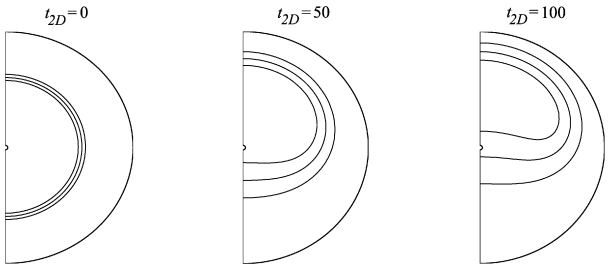

Fig. 28. Evolution of an initially circular drop with $a = 0.3$, $\delta_0 = 0.01$, $R = 2.3$ and $Ra = 10^5$. The drop deforms as it approaches the upper wall.

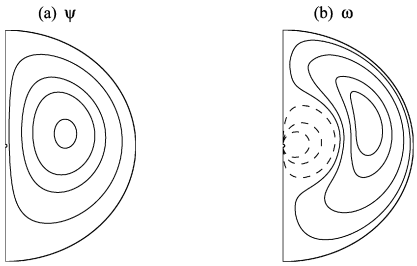

Fig. 29. (a) Streamfunction and (b) vorticity contours of the flow shown in Fig. 28 at $t = 50$.

cross-sectional plane, which motivates us to conduct a more general parametric study of this type, in order to explore the possible existence of a gravitational instability that could result in the experimentally observed splitting.

5.3. Evolution of initially circular drops

We now conduct a general parametric study of the two-dimensional evolution of drops in a cross-section of the tube. Note that these cross-sectional simulations involve the additional parameters a and δ. As a representative case, Fig. 28 depicts the temporal evolution of an initially circular drop for $a = 0.3$, $\delta_0 = 0.01$, $R = 2.3$ and $Ra = 10^5$. The concentration contours indicate that the drop deforms from its initial shape as it approaches the upper wall. Its interface is being stretched on top, while it thickens considerably in the rear of the drop. The accompanying streamfunction ψ and vorticity $\omega = -\nabla^2\psi$ plots are shown in Fig. 29. There is no indication of a gravitational instability resulting in a splitting of the drop.

In order to search for the existence of a gravitational splitting instability, we conducted a parametric study whose results are summarized in Fig. 30. As a diagnostic indicator, the figure shows the distance of the $c = 0.5$ contour from the upper wall as a function of time, for the reference parameter values of $a = 0.125$, $\delta_0 = 0.01$, $Ra = 10^8$ and $R = 2.3$. None of the simulations exhibited an instability of the kind sketched in Fig. 23. Within the parameter range explored here, R, Ra and δ have only a minor effect on the rise of the drop, which is dominated by the initial radius a.

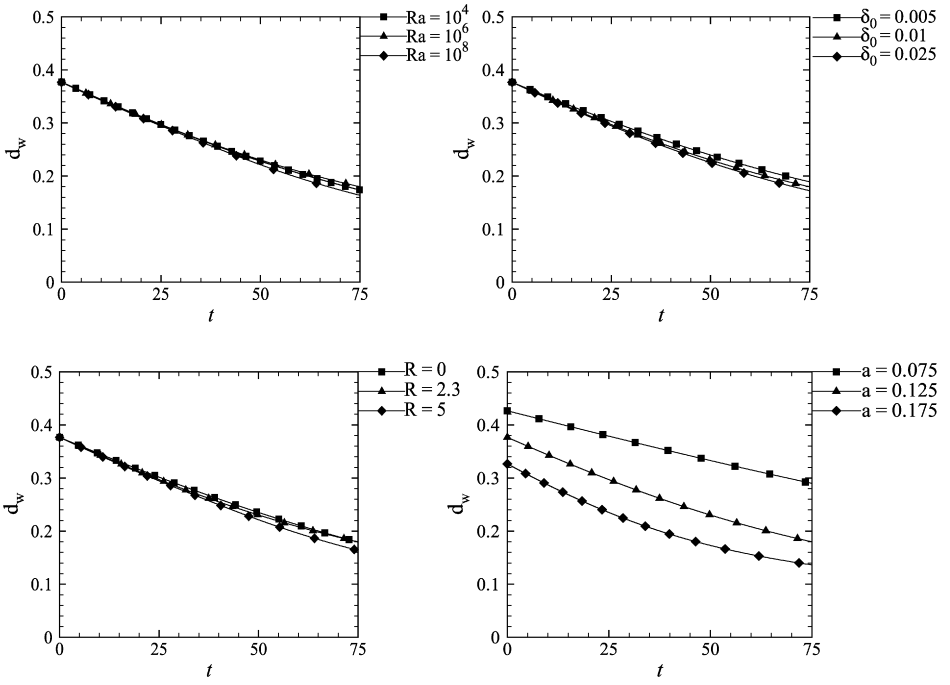

Fig. 30. Distance of the $c = 0.5$ contour from the upper wall as a function of time. Unless stated otherwise, $a = 0.125$, $\delta_0 = 0.01$, $Ra = 10^8$ and $R = 2.3$. The rise of the drop is dominated by its initial radius a, whereas the influence of the other parameters is small.

6. Conclusions

Axisymmetric and three-dimensional Stokes simulations of miscible displacements in horizontal capillary tubes have been conducted, in order to resolve discrepancies between simulations by [11] and corresponding experiments of [1] and [12]. An initial set of axisymmetric simulations addresses the influence of different viscosity–concentration relations on the quasisteady finger tip velocity. The results indicate that steeper relations generally result in a higher tip velocity. However, the effect is too small to provide an explanation for the observed discrepancies. Further axisymmetric simulations show that a concentration-dependent diffusion coefficient results in a slight reduction of the tip velocity at moderate *Pe*, but again the effect is too small to fully account for the observed differences between the constant diffusion coefficient simulations of [11] and the experiments of [1] and [12].

Three-dimensional simulations that account for gravitational forces in displacement flows within horizontal capillary tubes yield a much more significant effect. The qualitative finger shapes are in good agreement with the corresponding experimental observations. Beyond a certain value of the gravity parameter F, a quasi-steady state generally is not attained. This value of F increases with *Pe*. Consistent with the experiments of [1] and [12], at moderate *Pe* the tip slows down as the gravity parameter increases, an effect that becomes more pronounced as *Pe* decreases. The quantitative agreement between three-dimensional simulations and experiments is significantly better than for the earlier, axisymmetric simulations of [11], although some differences remain. In conclusion, the simulations demonstrate that three-dimensionality triggered by gravitational forces does provide a slowdown of the correct order of magnitude. We also note that there appears to be the possibility that the lowest experimentally reported tip velocity data do not reflect truly quasisteady states.

In the absence of information about the experimental parameter combination at which the splitting phenomenon was observed, we have been unable to reproduce this feature in our simulations. In order to check for the existence of gravitational instabilities that might cause such a splitting, we conducted additional two-dimensional simulations in cross-sections of the tube. A comparison of these two-dimensional results with corresponding three-dimensional simulations demonstrates that for a wide range of parameters the evolution of the trailing finger sections is governed by a two-dimensional balance between gravitational and viscous forces. However, a gravitational instability along the lines suggested by [1] was not observed in the cross-sectional simulations. On the other hand, in some of the

three-dimensional simulations the formation of a dimple was observed on the lower side of the finger, a short distance behind the tip. This dimple could possibly be a precursor to a full splitting event that may evolve after longer times. Taken together, the two- and three-dimensional simulations suggest that the splitting phenomenon observed by [1] more likely may be caused by the gravity-induced modification of the flow around the tip of the finger, rather than by a gravitational instability per se. Moreover, the splitting may originate on the underside of the finger, rather than at its upper boundary. However, a full resolution of this issue will require additional experiments and/or three-dimensional simulations.

Acknowledgements

We thank Dr. Dirk Wilhelm and Prof. G.M. Homsy for several helpful discussions. Also, the input of Prof. Tony Maxworthy, Dr. Philippe Petitjeans and Dr. Jun Kuang is gratefully acknowledged, as are the discussions with Dr. Nisheet Goyal on several computational issues. Support for this research was received from the NASA Microgravity and NSF/ITR programs, as well as from the Department of Energy and the UC Energy Institute, and through an NSF equipment grant. All calculations were performed on UCSB's CNSI and IGERT Linux clusters, and on TeraGrid resources provided by the San Diego Supercomputer Center.

References

[1] P. Petitjeans, T. Maxworthy, Miscible displacements in capillary tubes. Part 1. Experiments, J. Fluid Mech. 326 (1996) 37.
[2] J. Scoffoni, E. Lajeunesse, G.M. Homsy, Interface instabilities during displacements of two miscible fluids in a vertical pipe, Phys. Fluids 13 (3) (2000) 553.
[3] R. Balasubramaniam, N. Rashidnia, T. Maxworthy, J. Kuang, Instability of miscible interfaces in a cylindrical tube, Phys. Fluids 17 (10) (2005) 052103.
[4] G.M. Homsy, Viscous fingering in porous media, Annu. Rev. Fluid Mech. 19 (1987) 271.
[5] P.G. Saffman, Viscous fingering in Hele–Shaw cells, J. Fluid Mech. 173 (1986) 73.
[6] G.I. Taylor, Deposition of a viscous fluid on the wall of a tube, J. Fluid Mech. 10 (1960) 161.
[7] B.G. Cox, On driving a viscous fluid out of a tube, J. Fluid Mech. 14 (1962) 81.
[8] D.A. Reinelt, P.G. Saffman, The penetration of a finger into a viscous fluid in a channel and tube, SIAM J. Sci. Statist. Comput. 6 (1985) 542.
[9] E.J. Soares, M.S. Carvalho, P.R. Souza Mendes, Immiscible liquid–liquid displacement in capillary tubes, J. Fluids Engrg. 127 (1) (2005) 24–31.
[10] E.J. Soares, M.S. Carvalho, P.R. Souza Mendes, Gas-displacement of non-Newtonian liquids in capillary tubes, Inter. J. Heat and Fluid Flow 27 (1) (2006) 95–104.
[11] C.Y. Chen, E. Meiburg, Miscible displacements in capillary tubes. Part 2. Numerical simulations, J. Fluid Mech. 326 (1996) 57.
[12] J. Kuang, T. Maxworthy, P. Petitjeans, Miscible displacements between silicone oils in capillary tubes, Eur. J. Mech. B Fluids 22 (2003) 271–277.
[13] J. Kuang, T. Maxworthy, P. Petitjeans, Velocity fields and streamline patterns of miscible displacements in cylindrical tubes, Exp. Fluids 37 (2004) 301–308.
[14] J. Kuang, T. Maxworthy, The effects of thermal diffusion on miscible, viscous displacement in a capillary tube, Phys. Fluids 15 (4) (2003) 1340–1343.
[15] N. Rashidnia, R. Balasubramaniam, Measurement of the mass diffusivity of miscible liquids as a function of concentration using a common path shearing interferometer, Exp. Fluids 36 (2004) 619.
[16] R.F. Probstein, Physicochemical Hydrodynamics, second ed., John Wiley & Sons, Inc., 1994.
[17] D. Korteweg, Sur la forme que prennent les équations du mouvement des fluides si l'on tient compte des forces capillaires causées par des variations de densité, Arch. Neel. Sci. Ex. Nat. II (1901) 6.
[18] H. Hu, D. Joseph, Miscible displacement in a Hele–Shaw cell, Z. Angew. Math. Phys. 43 (1992) 626.
[19] J.B. Segur, Physics Properties of Glycerol and its Solutions, Reinhold, New York, 1953.
[20] Z. Yang, Y.C. Yortsos, Asymptotic solutions of miscible displacements in geometries of large aspect ratio, Phys. Fluids 9 (2) (1997) 286.
[21] O. Manickam, G.M. Homsy, Stability of miscible displacements in porous media with nonmonotonic viscosity profiles, Phys. Fluids 5 (6) (1993) 1356.
[22] D.D. Joseph, Fluid dynamics of two miscible liquids with diffusion and gradient stresses, Eur. J. Mech. B Fluids 9 (6) (1990) 565–596.
[23] D.D. Joseph, A. Huang, H. Hu, Non-solenoidal velocity effects and Korteweg stresses in simple mixtures of incompressible liquids, Physica D 97 (1996) 104.
[24] H. Davis, A theory of tension at a miscible displacement front, in: Numerical Simulation in Oil Recovery, in: IMA Volumes in Mathematics and its Applications, vol. 11, Springer, New York, 1988.
[25] C.Y. Chen, E. Meiburg, Miscible displacements in capillary tubes: Influence of Korteweg stresses and divergence effects, Phys. Fluids 14 (7) (2002) 2052.
[26] D. Wilhelm, E. Meiburg, Three-dimensional spectral element simulations of variable density and viscosity, miscible displacements in a capillary tube, Computers and Fluids 33 (3) (March 2004) 485–508.

[27] M.O. Deville, P.P. Fischer, E.H. Mund, High-Order Methods for Incompressible Fluid Flow, first ed., Cambridge University Press, 2002.
[28] U.M. Ascher, S.J. Ruuth, B.T.R. Wetton, Implicit explicit methods for time-dependent partial differential equations, SIAM J. Numer. Anal. 32 (3) (1995) 797–823.
[29] Y. Maday, A.T. Patera, E.M. Ronquist, An operator-integration-factor splitting method for time-dependent problems: Application to incompressible fluid flow, J. Sci. Comput. 5 (1990) 263–292.
[30] S.H. Vanaparthy, E. Meiburg, D. Wilhelm, Density-driven instabilities of miscible fluids in a capillary tube: linear stability analysis, J. Fluid Mech. 497 (2003) 99–121.
[31] M. Payr, S.H. Vanaparthy, E. Meiburg, Influence of variable viscosity on density-driven instabilities in capillary tubes, J. Fluid Mech. 525 (2005) 333–353.
[32] R.L. Chouke, Stability analysis for a secondary miscible displacement with an initially sharp solvent-oil interface, in: D.L. Dower, M.Y. Hussaini (Eds.), Proc. of the Society of Petroleum Engineers/Department of Energy Third Joint Symposium on Enhanced Oil Recovery, Springer, 1982, pp. 43–57.
[33] D.L. Tiffin, V.J. Kremesec, A mechanistic study of gravity-assisted co flooding, Presented at SPE/DOE 5th Symp. on Enhanced Oil Recovery, Tulsa, Oklahoma, April 20, SPE/DOE 14895, 1986.
[34] F.J. Fayers, T.J. Newley, Detailed validation of an empirical model for viscous fingering with gravity effects, Soc. Petrol. Eng. Reservoir Engrg. 3 (1) (May 1988) 542–550.
[35] D. Schafroth, N. Goyal, E. Meiburg, Non-monotonic viscosity variations in horizontal Hele–Shaw miscible displacement flows, Eur. J. Mech. B/Fluids 26 (2007) 444.
[36] A. Riaz, C. Pankiewitz, E. Meiburg, Linear stability of radial displacements in porous media: Influence of velocity-induced dispersion and concentration-dependent diffusion, Phys. Fluids 16 (10) (2004) 3592.
[37] S.H. Vanaparthy, C. Barthe, E. Meiburg, Density-driven instabilities in capillary tubes: Influence of a variable diffusion coefficient, Phys. Fluids 18 (4) (2006) 048101.
[38] N. Goyal, E. Meiburg, Miscible displacements in Hele–Shaw cells: Two-dimensional base states and their linear stability, J. Fluid Mech. 516 (2006) 211.
[39] T. Davis, Umfpack version 4.3 user guide, Technical report, 2004.
[40] S.K. Lele, Compact finite difference schemes with spectral-like resolution, J. Comp. Phys. 103 (1992) 16.
[41] A. Wray, Minimal storage time advancement schemes for spectral methods, Preprint, 1991.